# Numerical Methodologies for Magnetohydrodynamic Flow Control for Hypersonic Vehicles

Heather Muir(✉), Louisa Michael, and N. Nikiforakis

Department of Physics, Cavendish Laboratory, University of Cambridge, J J Thomson Avenue, Cambridge CB3 0HE, UK
ham38@cam.ac.uk

**Abstract.** The concept of magnetohydrodynamic (MHD) flow control is of current interest for its applications in spacecraft reentry and aerodynamic control for hypersonic vehicles. This work presents an efficient approach for realistically simulating MHD effects in weakly ionised plasmas produced by hypersonic flows. The governing equations consists of the full Navier-Stokes resistive-MHD system under the low magnetic Reynold's number assumption. The numerical approach employs a Cartesian mesh which facilitates hierarchical adaptive mesh refinement in a highly parallelised framework. Geometry is implemented via a rigid-body Ghost Fluid Method which permits arbitrarily complex embedded boundaries. An advanced 19-species equilibrium air-plasma equation of state (plasma19) has been adopted and extended in this work, for the study of test cases where the assumption of local thermodynamic equilibrium applies. The numerical methodology paired with plasma19 equation of state is shown to effectively capture boundary-layer shock wave interactions in a complex double-cone flow, with imposed magnetic field. The model predicts MHD flow control (augmented shock position) in line with experimental measurements, improving upon previous model predictions.

**Keywords:** Computational physics · Hypersonics · Magnetohydrodynamics · Flow control

## 1 Introduction

During hypersonic flight, the conversion of kinetic to thermal energy across the leading shock wave results in severe compression and heating of the gas surrounding the vehicle. Temperatures become so extreme that dissociation and ionisation reactions produce a weakly ionised plasma. This plasma layer has interesting properties which present both challenges and opportunities.

Given that the plasma layer is characterised by heightened electrical conductivity, this property can be innovatively leveraged. An imposed magnetic field generated from within the vehicle is able to exert a Lorentz force on the electrically conductive gas. The Lorentz force acts to increase shock stand-off distance,


R. King and D. Peitsch (Eds.): AFCC 2021, NNFM 152, pp. 336–355, 2022.
https://doi.org/10.1007/978-3-030-90727-3_21

in turn increasing total drag, reducing heat flux to the vehicle and reducing the density of free electrons. This collective mechanism of desirable effects is termed *MHD flow control*.

MHD flow control has a growing number of established and prospective applications. These include active thermal protection systems and the possibility of mitigating radio-black during spacecraft reentry, as well as aerodynamic control including hypersonic inlet control for ramjets and scramjets [1].

Numerous studies have demonstrated the effect of the gas chemistry model on the numerical simulation of weakly ionised plasmas formed from hypersonic flows [2–4]. The choice of gas chemistry model depends both on the ease of computation and on the validity range of its thermochemical assumptions. Additionally, for MHD applications, the computation of electric properties (such as electrical conductivity, and electron number density) are directly linked to the gas chemistry model and of especially high importance.

Studies on MHD control which adopt an ideal gas with supplementary finite conduction model are useful for investigating the flow effects of interest i.e. *relative* influence of Hall effect or magnetic field strength on the flow field, however, the *outright* results are unrealistic for the post-shock temperatures produced in hypersonic flows. Therefore, for MHD control feasibility to be realistically studied, a real gas model is required.

Real gas effects are captured by thermochemistry models which consider the dissociation and ionisation reactions occurring in high temperature air. In the context of reentry vehicles, with consideration of vehicle geometry and altitude-based free stream conditions, a map of valid thermochemical assumptions has been compiled as Fig. 1 from various data sources.

It is recognised that for a large portion of reentry trajectories the gas chemistry is in - or very close to - local thermochemical equilibrium (LTE) [5]. Figure 1 shows that the more ballistic the reentry trajectory the greater the portion of flight occurs under equilibrium conditions. A number of other MHD flow control applications also fall within the LTE valid regime. The major advantage of an equilibrium chemistry model is the use of pre-computed thermodynamic state data to efficiently obtain properties, and whereby the fluid dynamic time step need not be restricted due to the chemistry. A study by Chalot et al. [3] concluded that with optimum implementation, equilibrium chemistry programs may achieve a computing time close to only 20% slower than ideal gas.

As highlighted, the accurate computation of electrical conductivity underpins the realistic study of MHD effects. Bisek [9] also highlights that accurate conductivity modeling in the LTE regime typically involves supplementary models with semi-empirical approximations and remains problematic. As such, MHD effects have scarcely been studied in the equilibrium regime.

D'Angola *et al.* have made significant advances in computing the transport and thermodynamic properties of air plasmas in LTE [10,11]. This theory has formed the basis for the development of a new 19-species equilibrium air-plasma model (plasma19) by Treüble [12] which has been adopted and extended in this work.

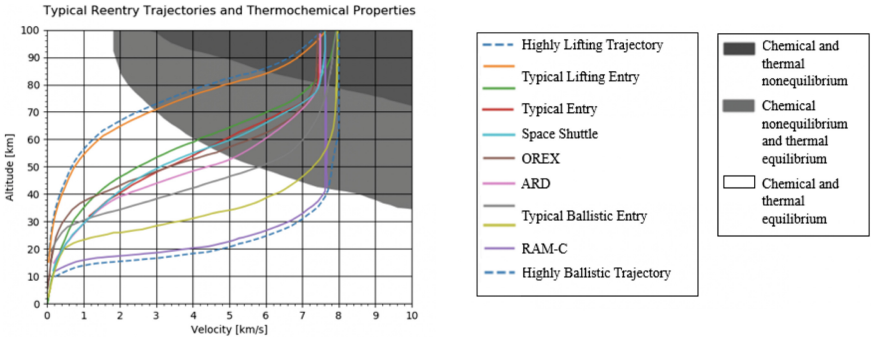


**Fig. 1.** Plot demonstrating regions of valid thermochemical assumptions, with overlaid reentry trajectories given by velocity-altitude coordinates. The zones of equilibrium states are as classified by Fujino *et al.* [6] for a spherical reentry vehicle of characteristic length O(1). The set of reentry trajectories is adapted from reference trajectory data from [7,8].

This work therefore proposes a computationally efficient approach for the realistic simulation of plasma generation and MHD effects in weakly ionised air-plasma within the equilibrium validity range. A full Navier-Stokes resistive-MHD system is modelled with real plasma gas effects, where electromagnetic properties including electron number density and electrical conductivity are computed directly, without need for supplementary approximation models. The numerical approach of this work combines methodologies which are able to realistically and efficiently capture complex flow interactions produced by non-simple geometries with viscous effects, under the influence of magnetic fields. To demonstrate the efficacy of this approach, this paper presents key validation cases for MHD Lorentz forcing dynamics, and for hypersonic double cone experiments. Model predictions are then compared to experimental results for a hypersonic double cone test case with imposed magnetic effects.

## 2 Governing Equations

### 2.1 Resistive MHD System Equations

The magnetohydrodynamic behaviour in this regime of flight is complex, with many interdependent phenomena across disparate scales. For numerical solution to be amenable, assumptions and simplifications are necessary.

In the case of aerospace plasmas - where collision frequency within the plasma is sufficiently high, flow length scales are significantly larger than the Debye length, and time scales are larger than the reciprocal of the plasma resonant frequency - a continuum magnetohydrodynamic (MHD) model governs [13].

Broadly across the literature, hypersonic plasmas are considered in the low magnetic Reynolds number regime [1,6,14] where $Re_m$ is of the order of unity or

less. Under this regime the imposed and induced magnetic fields are sufficiently decoupled such that the static imposed magnetic field is unaffected by the flow.

$$Re_m = \frac{\text{Magnetic induction}}{\text{Magnetic diffusion}} = \frac{\sigma_0 V_0 L_0}{\epsilon_0 c^2} \tag{1}$$

The governing system equations are derived by combining the Navier-Stokes equations for fluid dynamics (accounting for fluid viscosity and thermal conductivity) with Maxwell's equations for electromagnetism. The derivation under the low $Re_m$ weakly ionised plasma regime results in resistive MHD equations which account for Lorentz forcing and joule heating.

For studies of axisymmetric vehicle geometries, the axis of symmetry can be exploited, converting the 3D problem into a 2D plane in cylindrical coordinates. And therefore the MHD system equations are given in r-z space as:

$$\frac{\partial \mathbf{U}}{\partial t} + \frac{\partial \mathbf{F}}{\partial r} + \frac{\partial \mathbf{G}}{\partial z} = \frac{\partial \mathbf{F}_v}{\partial r} + \frac{\partial \mathbf{G}_v}{\partial z} + \mathbf{S}^c + \mathbf{S}_v^c + \mathbf{S}_{MHD} \tag{2}$$

$\mathbf{U}$, $\mathbf{F}$ and $\mathbf{G}$ denote the state vector, and r-z directional inviscid flux vectors respectively, and $\mathbf{S}^c$ denotes the associated cylindrical source term vector. For the 2D r-z system, we denote the velocity vector in the $(\hat{r}, \hat{z}, \hat{\theta})$ direction to have components $(u, v, w)$, and so the system vectors are defined as:

$$\frac{\partial \mathbf{U}}{\partial t} = \begin{pmatrix} \rho \\ \rho u \\ \rho w \\ \rho v \\ E \end{pmatrix}_t \quad \frac{\partial \mathbf{F}}{\partial r} = \begin{pmatrix} \rho u \\ \rho u^2 + p \\ \rho uw \\ \rho uv \\ u_r(E+p) \end{pmatrix}_r \quad \frac{\partial \mathbf{G}}{\partial z} = \begin{pmatrix} \rho w \\ \rho uv \\ \rho vw \\ \rho v^2 + p \\ v(E+p) \end{pmatrix}_z \quad \mathbf{S}^c = \begin{pmatrix} -\frac{1}{r}\rho u \\ -\frac{1}{r}\rho u^2 \\ -\frac{1}{r}\rho uw \\ -\frac{1}{r}\rho uv \\ -\frac{1}{r}u(E+p) \end{pmatrix} \tag{3}$$

where total energy $E$ is given by: $E = \rho e + \frac{1}{2}\rho \mathbf{u}^2$.

Assuming a Newtonian fluid, the viscous stress tensor is given by:

$$\boldsymbol{\tau} = \mu(\nabla \mathbf{u} + \nabla \mathbf{u}^T) + \lambda(\nabla \cdot \mathbf{u})I \tag{4}$$

where $\mu$ is the fluid dynamic viscosity and using stokes hypothesis $\lambda = -\frac{2}{3}\mu$. $\zeta$ is the fluid's thermal conductivity.

The flow is assumed to be laminar, and dynamic viscosity is computed via Sutherland's law. Thermal conductivity is computed with constant Prandtl number = 0.71 for the ideal gas case, and $\zeta$ has precomputed state data in the plasma19 gas model.

then the viscous flux vectors are derived as follows:

$$\frac{\partial \mathbf{F}_v}{\partial r} = \begin{pmatrix} 0 \\ \tau_{rr} \\ \tau_{rz} \\ \tau_{r\theta} \\ Q_r \end{pmatrix}_r = \begin{pmatrix} 0 \\ \mu(\frac{4}{3}u_r - \frac{2}{3}v_z - \frac{2}{3}\frac{u}{r}) \\ \mu(v_r + u_z) \\ \mu(w_r - \frac{w}{r}) \\ u\tau_{rr} + v\tau_{rz} + w\tau_{r\theta} + \zeta T_r \end{pmatrix}_r \tag{5}$$

$$\frac{\partial \mathbf{G}_v}{\partial z} = \begin{pmatrix} 0 \\ \tau_{zr} \\ \tau_{zz} \\ \tau_{z\theta} \\ Q_z \end{pmatrix}_z = \begin{pmatrix} 0 \\ \mu(u_z + v_r) \\ \mu(\frac{4}{3}v_z - \frac{2}{3}u_r - \frac{2}{3}\frac{u}{r}) \\ \mu w_z \\ u\tau_{zr} + v\tau_{zz} + w\tau_{z\theta} + \zeta T_z \end{pmatrix}_z \tag{6}$$

and the following viscous source term vector emerges from the cylindrical system conversion:

$$\mathbf{S}_v^c = \begin{pmatrix} 0 \\ \tau_{rr} - \tau_{\theta\theta} \\ \tau_{rz} \\ \tau_{r\theta} \\ Q_r \end{pmatrix} = \begin{pmatrix} 0 \\ \frac{2}{r}\mu(u_r - \frac{u}{r}) \\ \frac{1}{r}\mu(u_z + v_r) \\ \frac{2}{r}\mu(w_r - \frac{w}{r}) \\ \frac{1}{r}(u\tau_{rr} + v\tau_{rz} + w\tau_{r\theta} + \zeta T_r) \end{pmatrix} \tag{7}$$

Some additional assumptions and resultant simplifications can be made in defining the $\mathbf{S}_{MHD}$ vector.

The full expansion of Ohm's law includes a Hall current contribution. This additional current drives the generation of an electric field which has a complex interaction with the gas dynamics - termed *Hall effect*. Several authors have shown that for a conductive body, the Hall effect diminishes the MHD flow control [15]. In the case of a perfectly insulated body, however, the overall flow structure is essentially unaffected by the Hall effect [16,17]. Regarding the leading surfaces as an insulated material (via the electrodynamic boundary condition at the body), studies of MHD flow control justifiably neglect Hall effect [18–20], therefore applying the *generalised* Ohm's law as given by Eq. 8:

$$\mathbf{J} = \sigma(\mathbf{E} + \mathbf{u} \times \mathbf{B}) \tag{8}$$

The electric field $\mathbf{E}$ is a conservative field where $\mathbf{E} = -\nabla\phi$ and $\phi$ is the electric potential. Therefore the governing system is comprised of system of 5 hyperbolic PDE's as defined within Eq. 2, coupled with an additional Poisson-type elliptic PDE maintaining divergence-free current density:

$$\nabla \cdot [\sigma(-\nabla\phi + \mathbf{u} \times \mathbf{B})] = 0 \tag{9}$$

The magnetic field is a static imposed dipole field with dimensional components $\mathbf{B} = (B_r, B_\theta, B_z)$, and defined analytically via:

$$\mathbf{B} = B_0 \left[ \frac{3\mathbf{r}(\mathbf{r} \cdot \mathbf{m}) - r^2\mathbf{m}}{r^5} \right] \tag{10}$$

Where $\mathbf{r}$ is the radial vector from the dipole centre, and $\mathbf{m}$ is an orientation vector aligned parallel to the dipole centreline. Within the axisymmetric governing system where $\mathbf{r}$ and $\mathbf{m}$ are defined in the r-z plane, the $B_\theta$ magnetic field component is zero.

For electrodynamic boundary conditions which treat the surface as insulated, the solution of equation of 9 can be solved analytically as $\phi = 0$, which means the

elliptic current density equation does not require numerical solution and electric current density is given by:

$$\mathbf{J} = -\sigma(u_r B_z - u_z B_R)\hat{\theta} = J_\theta \tag{11}$$

Therefore the Lorentz forcing terms in the MHD source term vector can be defined directly, rendering the computation as vastly more expedient:

$$\mathbf{S}_{MHD} = \begin{pmatrix} 0 \\ (\mathbf{J} \times \mathbf{B})\hat{r} \\ (\mathbf{J} \times \mathbf{B})\hat{\theta} \\ (\mathbf{J} \times \mathbf{B})\hat{z} \\ \mathbf{u} \cdot (\mathbf{J} \times \mathbf{B}) + \sigma^{-1} J^2 \end{pmatrix} = \begin{pmatrix} 0 \\ -\sigma(u_r B_z^2 - u_z B_r B_z) \\ 0 \\ \sigma(u_r B_z B_r - u_z B_r^2) \\ u_r J_\theta B z - u_z J_\theta B_r + \sigma^{-1} J^2 \end{pmatrix}$$

### 2.2 Plasma19 Equation of State

This work employs an advanced equation of state (EoS) for an air plasma which considers 19-species reaching chemical and thermal equilibrium. The new *plasma19* EoS leverages a precomputed database recently developed by Träuble in 2021 [12] (utilising theory from D'Angola [10] and Colonna [21]). This database has been extended in this work over a wider density-pressure range necessary for atmospheric reentry conditions, and with an extended implementation for electron number density in line with the extended theory of D'Angola [11].

The 19-species considered in the air-plasma are:

$$N_2,\ N_2^+,\ N,\ N^+,\ N^{++},\ N^{+++},\ N^{++++},$$
$$O_2\ ,\ O_2^+,\ O_2^-,\ O,\ O^-,\ O^+,\ O^{++},\ O^{+++},\ O^{++++},$$
$$NO,\ NO^+,\ e^-$$

The molar fractions of each chemical species, and bulk thermodynamic properties under equilibrium are precomputed in this database through a Gibbs free energy minimisation method (solved numerically through for e.g. Newton-Raphson iterative scheme). The full set of state properties computed by Plasma19 have been extensively validated against empirical measurements [12].

In the state database previously generated the electron species molar fraction was found to become unreliable below approximately 10,000 K. This was insufficient for the temperature band of interest for hypersonically generated plasmas (approximately 2,000 K–10,000 K). In recognising this issue, D'Angola's proposed a theoretical formulation for electron molar fraction in the extended work [11], which is verified to compute "very accurate" electron molar fraction in air plasmas down to temperatures as low as 50 K. Therefore this theoretical formulation was implemented in this work to generate an extended plasma19 state database, achieving direct and accurate resolution of electron number density over the full property range of interest for equilibrium aerospace plasmas (verified against the results of D'Angola [11]).

For MHD studies, it is critical for the EoS to accurately compute electrical conductivity based on species dissociations and ionisations at the relatively low

air-plasma temperature resulting from this regime. The negatively charged $O^-$ and $O_2^-$ species are not captured by an 11-species model but are computed to be present in small concentrations in the air-plasma temperature band of interest.

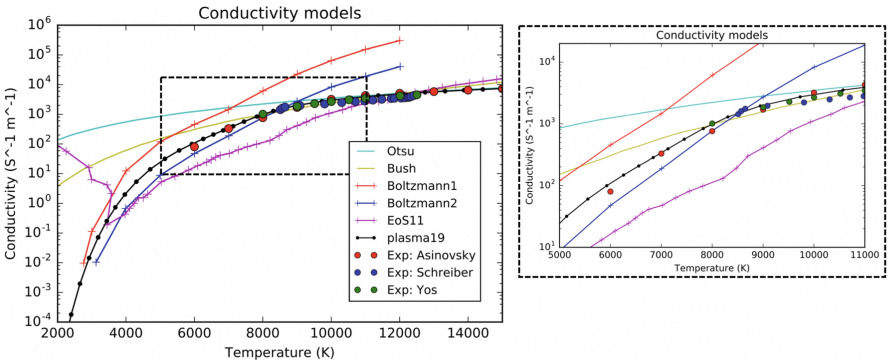


**Fig. 2.** Electrical conductivity across low air-plasma temperature range at pressure = 1 atm. Comparison of $\sigma$ computed by plasma19 with other models currently used in the literature and to experimental measurements (refer to text).

Comparison of the computed electrical conductivity across the extended plasma19 validity range shows very good agreement with experimental measurement - critically, in the low temperature range typical of hypersonic flight in the LTE regime. In Fig. 2, three sets of experimental measurements have been obtained from the works of Asinovsky et al. (1973) [22], Schreiber et al. (1971) [23] and Yos (1963) [24] where a low-temperature equilibrium plasma was generated via a stabilised DC arc applied to a column of air maintained at atmospheric pressure. Otsu [16] and Bush [25] use the simple analytic power law approximation defined in next section's Eq. 15 with exponents 2 and 4 respectively. It is clear that the analytic approximations used by Otsu and Bush produce reasonable estimations at temperatures above approximately 9,000 K, but diverge from experimental measurements as temperature decreases. Boltzmann solvers for electrical conductivity involve the complex solution of a large set of coupled ODEs and are computationally expensive. EoS11 is an 11-species equilibrium model as implemented by Villa et al. [26]. As can be seen, the non-physical species molar fractions over the low temperature range, and resultant anomalous electrical conductivity, render EoS11 as problematic for LTE MHD studies. The anomalous conductivity values at low temperatures are not only physically unrealistic, but sharp jumps in properties lead to numerical instability when integrating the MHD forcing source terms.

The efficiency of the overall code depends strongly on the efficiency of the interpolation access routine for the look-up table. Therefore, this work implements an efficient binary search method - finding indices in O(log(n)) operations - with bilinear interpolation between the state data of the tabulated indices.

Plasma19 has the advantage of leveraging the pre-computed $\sigma$ values without the need for a supplementary conductivity formulation, rendering the model as highly efficient. The smooth and accurate conductivity values computed by plasma19 over the low temperature range enable the direct and realistic simulation of LTE MHD flow control for this regime.

## 3 Numerical Methods

The model of this work is a new research code developed within the AMReX framework [27]. The underlying computational mesh is regular Cartesian with hierarchical adaptive mesh refinement (AMR), where the domain is subdivided into blocks as represented in Fig. 3. This framework permits massively parallel computation of the domain sub-blocks, resulting in efficient and highly scalable computation.

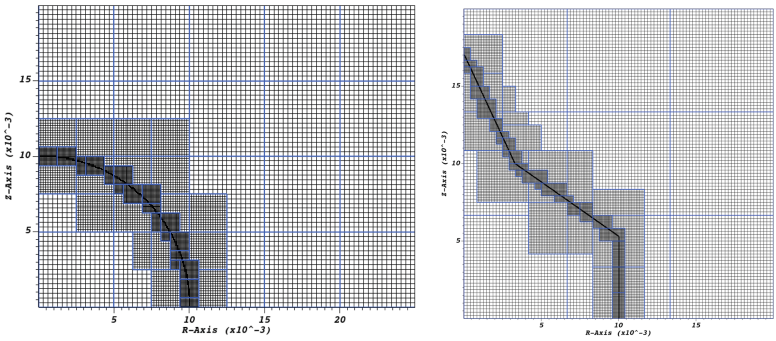


**Fig. 3.** Cartesian mesh configuration with two levels of hierarchical AMR. Blue borders show subdivision of the domain into 'blocks' which can be computed in parallel.

Geometry is implemented via a rigid body Ghost Fluid Method (GFM), such as that implemented by Bennett et al. [28], based on the approach of Sambasivan and UdayKarmar [29]. By implementing embedded boundary geometry via a rigid body GFM, the mesh is not subject to distortions and skewing which sometimes occur in the case of body fitted meshes, especially as geometries become more complex, and the adaptive refinement approach ensures high resolution is achieved automatically and locally in the vicinity of high density gradients. This combination of methods therefore permits the accurate, robust and efficient modeling of complex geometries in the presence of strong shocks, with multiple levels of hierarchical AMR applied to achieve high effective resolution and solved efficiently via MPI-based computation with high scalability across many nodes.

The system is solved via an operator split strategy whereby the hyperbolic and diffusive fluxes are computed successively with the result of each time-wise integration input as the initial condition for the subsequent operation.

Fluxes are also dimensionally split in this manner. Cylindrical and MHD source terms are integrated via simple Euler time step integrations.

The stable time-step is restricted as the minimum of the hyperbolic and diffusive stable time steps, given by:

$$\Delta t = \min[\Delta t_{hyp}, \Delta t_{diff}] \tag{12}$$

$$= \min[\frac{\text{CFL} \cdot \Delta x_{d,i}}{S_{max,i}}, \frac{(\Delta x_{d,i})^2}{2 \cdot \max[\frac{\mu_i}{\rho_i}, \frac{\zeta_i}{(\rho c_p)_i}]}] \tag{13}$$

where $\Delta x_{d,i}$ is each dimensional spatial step size. Under the operator split solution strategy the explicit time-marching evolution is stable in 2-dimensions and including all source terms for CFL = 0.9.

The hyperbolic system fluxes are evaluated numerically via a complete wave approximate Riemann solver (HLLC) with high order extension (MUSCL) which is second order accurate in space and first order accurate in time. Complete wave Riemann solvers are susceptible to the Carbuncle instability for test cases in the hypersonic regime. A shock detection with transverse flux stabilisation method is implemented for effective suppression of Carbuncle instability. The transverse flux stabilisation employs a weighted combination flux (complete and incomplete wave solver fluxes) in the vicinity of strong, normal, grid-aligned shocks - an approach which is similar to the HLLE++ method described by Tramel [30], but treated here as a directly augemented flux rather than system eigenvalue modification, and meliorated in this case to a Cartesian mesh with hierarchical AMR. Viscous derivative terms are evaluated using the central differencing method at cell interfaces with divergence then computed through the finite volume construction. The transient solver can be used for time accurate simulation of transient test cases, and also reaches a stable and convergent steady state (converges to equivalent result above sufficient resolution) for steady test cases.

## 4 Validation

### 4.1 MHD System Validation Under Ideal Gas Law

For the purpose of validating the underlying resistive MHD model, the model is first reduced to its inviscid Euler equivalent, closed with an ideal gas equation of state for comparison with the validation test cases in the literature. The most prevalent validation test is the case originally studied by Poggie & Gaitonde [18], and replicated subsequently by Damevin & Hoffmann [31] and most recently by Fujino et al. [32].

The free-stream conditions for the flow over a 10 mm radius sphere are:

$$\underline{\text{Free-stream conditions:}}$$
$$\text{M} = 5,\ \text{Re} = 80,000,\ T_\infty = 100\ \text{K},$$
$$V_\infty = 1002.25\ \text{m/s},\ \rho_\infty = 0.0798\, kg/m^3,\ p_\infty = 2290.85\ \text{Pa}$$

The MHD effect is shown to increase shock stand-off distance with increased magnetic interaction parameter ($Q_{MHD}$) defined as:

$$Q_{MHD} = \frac{\text{Lorentz force}}{\text{Fluid inertial force}} = \frac{\sigma_0 B_0^2 R_0}{\rho_\infty V_\infty} \tag{14}$$

where $\sigma_0$ is taken to be the maximum post-shock conductivity (in the stagnation region), $B_0$ is the maximum absolute magnetic field strength outside of the vehicle, and the characteristic length $R_0$ is the radius of the spherical body.

Since the gas conductivity is not captured by the ideal gas EoS, a supplementary analytic equation for conductivity is required. Models from various studies [14,16,18] assume an approximate conductivity model of the following form:

$$\sigma = \sigma_0 \left( \frac{T}{T_{ref}} \right)^n \tag{15}$$

where $T_{ref}$ is taken to be the maximum temperature in the stagnation region.

Poggie & Gaitonde investigate different valued exponents (n = 0–4), and conclude that the exponent, and conductivity model more generally, has a notable impact on the MHD control effects. For these initial set of validation tests they assume a constant conductivity of $\sigma_0 = 300(\Omega m)^{-1}$, i.e. n = 0, in the post-shock region. Magnetic field strength is varied corresponding to $Q_{MHD}$ values of 0–6.

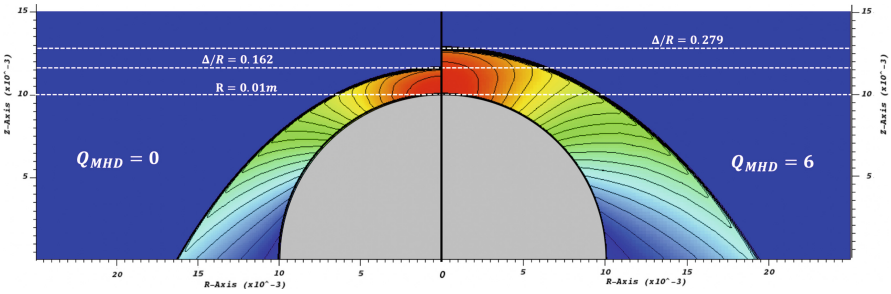


**Fig. 4.** Pressure profiles with contours as computed in this work for $Q_{MHD} = 0$ and $Q_{MHD} = 6$.

The full pressure profile for the $Q_{MHD} = 0$ and $Q_{MHD} = 6$ cases are shown in Fig. 4 and are in very good agreement with the literature. Examining the result quantitatively, Fig. 5 shows that the shock stand-off distances computed under 6 different magnetic field strengths exhibit excellent agreement with literature results and theory.

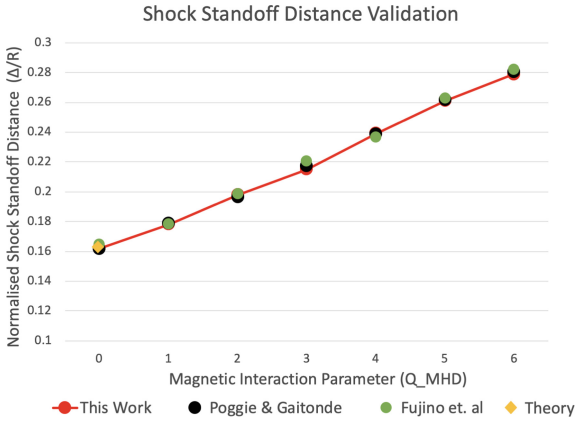


**Fig. 5.** Quantitative comparison of shock stand-off distance for this work vs previous studies for $Q_{MHD} = 0{-}6$.

### 4.2 Hypersonic Double Cone Tests

The hypersonic double cone tests are famously used for the validation of Navier-Stokes codes to model non-simple geometries and capture boundary layer shock wave interactions. Experimental data has been obtained from a large number of tests in the CUBRC LENS facilities [33] producing a high enthalpy, hypersonic, laminar flow with shock wave boundary layer interactions.

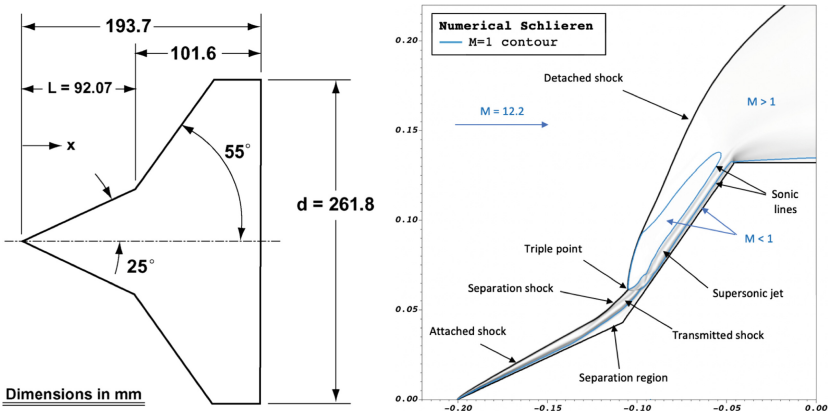


**Fig. 6.** Left: geometry specifications of the CUBRC 25/55° double cone model, right: numerical Schlieren result of this work from test conditions of the CUBRC run 1 flow.

Figure 6 shows the model dimensions for the CUBRC experiments, and a numerical Schlieren result of the run 1 conditions, demonstrating the ability of the Navier-Stokes rigid body GFM model to capture the complete feature formation at steady state.

To validate the system quantitatively a pressure trace is taken along the surface of the vehicle and compared with the results of the experiments and other simulations. The first case considers the test run 7 conditions for non-reactive nitrogen ($N_2$) gas.

$$\underline{\text{CUBRC run 7 conditions:}}$$
$$\text{M} = 15.6,\ V_\infty = 2073\ \text{m/s},\ T_\infty = 42.6\ \text{K},\ T_w = 300\ \text{K},$$
$$\rho_\infty = 1.57 \times 10^{-4}\, kg/m^3,\ p_\infty = 2.23\ \text{Pa},\ \text{Gas} = N_2$$

For other cases including air test runs, where real reactive gas effects are at play, perfect quantitative agreement between experiment and simulation remains illusive and has been the subject of many studies: [33–35] among others. Though all models struggle to exactly match experiments in terms of heat flux and pressure distribution, generally good agreement is found between numerical models. Zuo recently (2021) [36] showed that for runs with air as the test gas, similar results are obtained between perfect gas, thermochemical equilibrium and non-equilibrium models in terms of qualitative flow structure and surface properties. Another recent (2020) study by Holloway [37] showed that equilibrium and non-equilibrium models demonstrated reasonably good agreement in terms of overall shock structure and property fields for the air-gas composition test case.

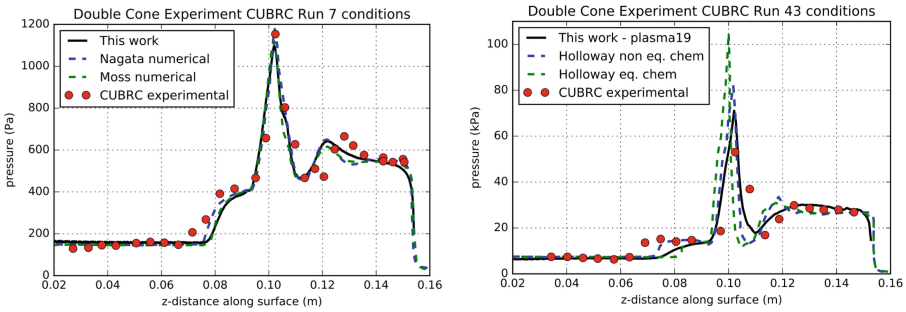


**Fig. 7.** Pressure trace along surface of double cone: left: CUBRC run 7 compared with experimental result and simulations of Nagata et al. [38] and Moss et al. [39], right: CUBRC run 43 compared with experimental result and simulations of Holloway [37] under different thermochemistry assumptions.

The air test case of CUBRC run 43 is studied by Holloway [37] and compares results for 11 species equilibrium and 11 species non-equilibrium (two-temperature) models. The quantitative results of these models are compared to the result of this work and the experimental data, as shown in Fig. 7.

$$\underline{\text{CUBRC run 43 conditions:}}$$
$$\text{M} = 8.87,\ V_\infty = 4267\ \text{m/s},\ T_\infty = 576\ \text{K},\ T_w = 296.2\ \text{K},$$
$$\rho_\infty = 2.134 \times 10^{-3}\, kg/m^3,\ p_\infty = 352.77\ \text{Pa},\ \text{Gas} = \text{Air}$$

Whilst none of the models perfectly capture the position of the transmitted shock upstream of the separation region, the result of this work shows very good

agreement with prevailing models which account for real gas effects. In fact the peak pressure and post-peak dip in pressure computed from this work are seen to match more closely with the experimental data. Properties along the secondary surface of the double done are more critical for the ensuing MHD double cone test, since magnetic interaction dominates downstream of the kink.

## 5 Results

### 5.1 Hypersonic Double Cone with Electrodynamic Effect

Wasai et al. [40] conducted an experiment on magnetohydrodynamic control of shock interactions over a 25°/55° double cone geometry (Fig. 8) in hypersonic flow where results were obtained to measure the MHD flow control effect. Simulations of the experimental conditions have been conducted by Nagata et al. [38,41].

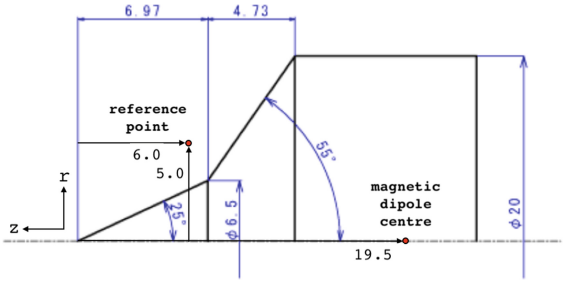


**Fig. 8.** Geometry specifications for the experiments of Wasai et al. [40] with dimensions in mm. The case of B = 0.36 T is the measured magnetic field strength at the reference point.

Results of their numerical simulations showed that for a magnetic field strength matched with the experimental condition the MHD effect was unobservable in the computed steady state flow field solution. However, the experiment does in fact reveal a small but observable increase in shock stand-off distance due to MHD flow control. By initialising the magnetic field strength in the numerical simulation to be much higher than that of the experiment, Nagata et al. were able to demonstrate the qualitative effect an imposed magnetic field has on the flow, which agrees with the qualitative effect observed in the experiment.

The experimental inflow test gas was pre-heated, and Wasai [40] and Nagata [41] consider it to have reached a state of thermochemical equilibrium, determining the initial (single) temperature and species composition as such. Experimental results for the test run of flow velocity of 11.6 km/s are presented by Wasai [40] and therefore used as the test flow condition for this work.

Test run conditions:

$$\mathrm{M} = 5.6,\ V_\infty = 11.6\ \mathrm{km/s},\ T_\infty = 6110\ \mathrm{K},\ T_w = 300.0\ \mathrm{K},$$
$$\rho_\infty = 2.52 \times 10^{-3}\, kg/m^3,\ p_\infty = 7.22\ \mathrm{kPa},\ \mathrm{Gas} = \mathrm{Air}$$

Importantly the flow is characterised with the following parameters:

$$\text{Reynolds number} = 1.77 \times 10^3$$
$$\text{Magnetic Reynolds number} = 0.2$$
$$\text{Hall parameter} = 0.61$$

Additionally, the model surface is treated as an insulated surface. Therefore it can be assessed that the governing model assumptions of low magnetic Reynolds number, and simplified Ohm's law neglecting Hall effect are valid for this test case.

The increase in shock stand-off position is observed via a brightness intensity rendering of the flow field with and without the imposed magnetic field, and also, by taking a trace through lines parallel to the z-axis of symmetry at different radial distances (r = 4 mm, 8 mm and 10 mm) along the model to determine shock position more precisely. These results are presented for the 11.6 km/s test case in reference [40], and the increase in leading shock position due to MHD effect of the imposed magnetic field is measured from these graphs, presented with uncertainty margins in the table of Fig. 9.

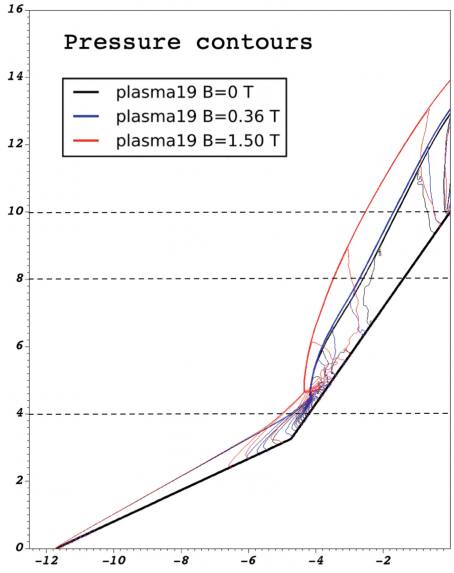


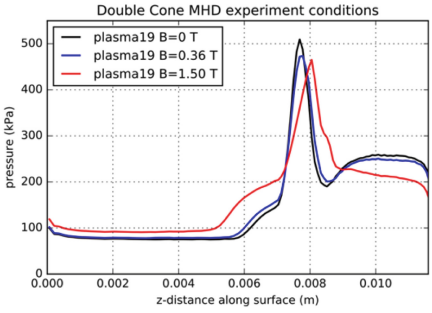


| Radial distance | MHD shock stand-off enhancement – Experiments (mm) | MHD shock stand-off enhancement – This work (mm) |
|---|---|---|
| R = 4 mm | 0.046 - 0.264 | 0.052 |
| R = 8 mm | 0.081 - 0.366 | 0.117 |
| R = 10 mm | 0.079 - 0.373 | 0.115 |

**Fig. 9.** Left: contours of pressure for the case without magnetic field, magnetic field initialised to experimental value B = 0.36 T, and a stronger magnetic field of B = 1.5 T intensity, with radial lines of 4 mm, 8 mm, 10 mm marked. Upper right: comparison of pressure trace along surface. Lower right: increase in shock stand-off distance from the series of experiments by Wasai et al. [40]- measured range of values from experimental graphs, compared with measured increase in leading shock stand-off distance computed from this work with experimental value of magnetic field strength B = 0.36 T.

In the table of Fig. 9, the measured increase in leading shock stand-off from the simulations of this work are compared to the measured increase from the trace taken along the radial lines in the results of Wasai et al. [40]. Results show an increase in shock stand-off distance in line with the range of results measured from the experiments. The shock stand-off enhancement effect can be visualised through the pressure contour plot of Fig. 9.

The MHD effect as depicted by the overlaid pressure contours for different magnetic field strength (Fig. 9) agrees very well in terms of qualitative phenomenology of the simulations Nagata et al. [38,41]. The change in pressure trace property along the vehicle surface also shows good qualitative agreement with traces computed by Nagata et al. Further, the predictions of this work are quantitatively in-line with experimental measurements for matched Magnetic field strength. Therefore, the model of this work appears highly suitable to capture realistic MHD flow control effects in hypersonic flows with complex geometries.

The model permits us to investigate many other properties of interest in the weakly ionised plasma layer formed around the vehicle, both in the absence of, and under the influence of, an applied magnetic field. A key property of interest for many applications is electron number density ($N_e$). Figure 10 shows the computed electron distribution for the case with and without magnetic field activated.

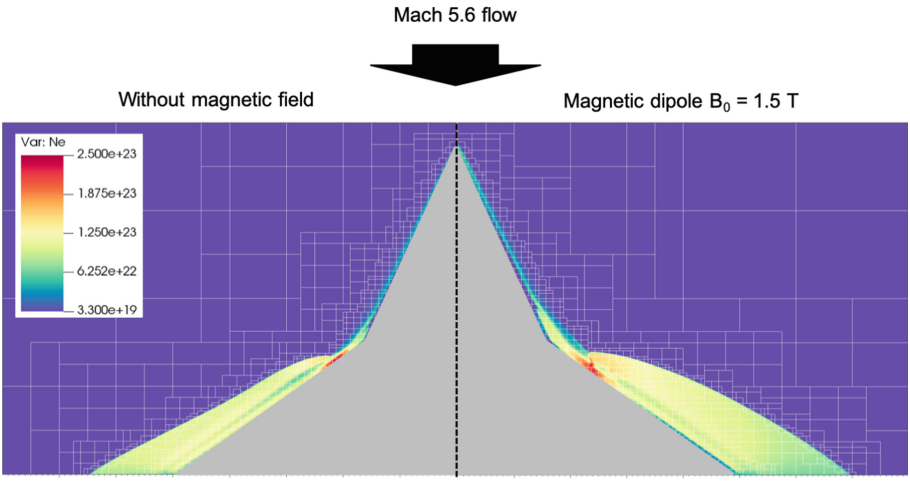


**Fig. 10.** Comparison of steady state solution for electron number density ($N_e$) without magnetic field (left plane) and for the case of applied magnetic field of strength B = 1.5 T. Regions of mesh refinement are shown by white block borders.

There are a number of additional electromagnetic properties which result directly from the activation of the magnetic field. Figure 11 shows (for the B = 1.5 T case) the induced electric current in the circumferential directions, revealing there exists an anticlockwise current flow in the supersonic shock regions of the flow structure and a clockwise current flow in the separation and subsonic regions. The Lorentz force magnitude with directional vector plot shows peak magnetic

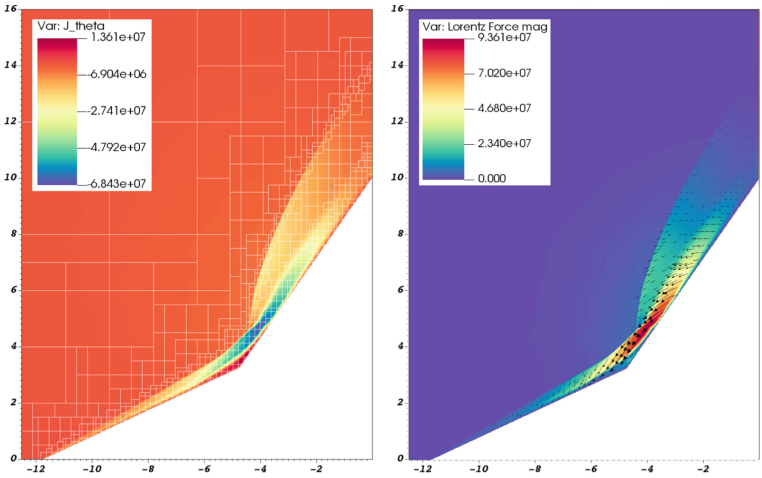


**Fig. 11.** Key electromagnetic properties- left: circumferential component of electric current density, and right: Lorentz forcing magnitude and directional vectors.

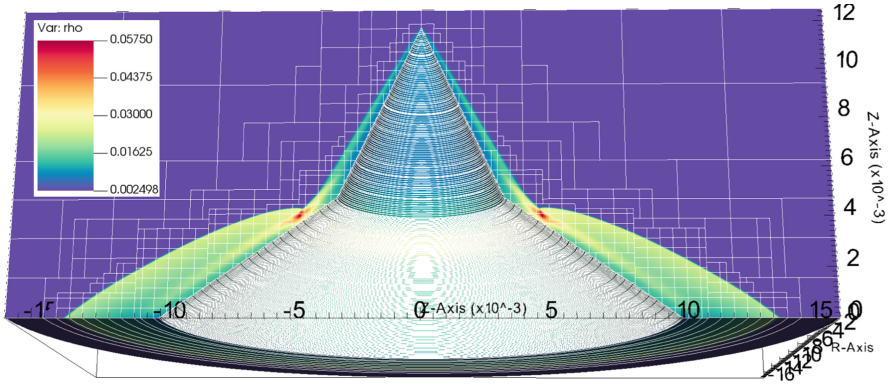


**Fig. 12.** Full 3D rendering of computed density field for case of imposed magnetic field strength B = 1.5 T.

forcing in the region of peak anticlockwise electric current flow. The directional vectors indicate why a notable movement in separation shock position was previously observed in the pressure contour plot. Resolving these parameters reveal useful insights for understanding the progression of shock structure phenomenology enacted by electrodynamic influence (Fig. 12). Since the magnetic interaction parameter is scaled by flow momentum, we see from this result that low velocity flow regions are determined as having high magnetic interaction.

Assessment of LTE Validity for MHD Effects

LTE validity is primarily determined by the comparison of the rate of chemical reaction to the rate of fluid transport. Specifically, in the case of quantifying MHD effects, the relevant consideration is that the system tends toward equilib-

rium specifically where the magnetic interaction is dominant. Therefore to assess the appropriateness of the LTE model for the MHD flow control double cone test case, the magnitude of magnetic interaction parameter (indicator of where the flow is electromagnetically affected by the imposed **B**-field) is compared with an indicative measure of fluid residence time ($\tau_r$), defined as:

$$\tau_r = \frac{\text{vehicle length scale}}{\text{total velocity}} = \frac{L_0}{|\mathbf{v}|} \tag{16}$$

Where the velocity approaches a very low magnitude (such as subsonic and stagnation regions), and therefore the residence time is high, the flow can be assumed to be approaching equilibrium. Figure 13 shows the comparison of defined $\tau_r$ and magnetic interaction parameter $Q$:

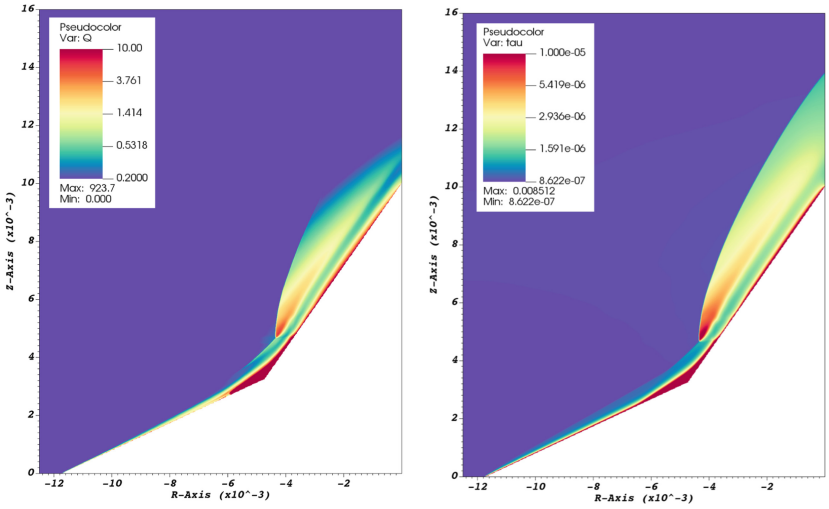


**Fig. 13.** Left) magnetic interaction parameter: $Q = (\sigma|B|^2 R_0)/(\rho|\mathbf{u}|)$, compared with right) residence time indicator of regions approaching equilibrium: $\tau_r = \frac{L_0}{|V|}$

As can be seen from the comparison in Fig. 13, the regions with dominant magnetic interaction, predominantly producing the measured MHD effects, map very well with the regions where the flow is expected to approach equilibrium based on the residence time indicator $\tau_r$. This is an important relationship to draw: regions which tend to zero velocity, also tend towards equilibrium in terms of the chemical state, and correlate with the key regions of the flow structure where the Lorentz forcing magnitude vs flow momentum is high such that electromagnetic forcing affects the flow.

## 6 Conclusions

This work reports on a new research code with a methodology for the realistic and efficient simulation of weakly ionised air plasmas in the LTE regime, and associated MHD phenomena. The Navier-Stokes resistive-MHD system (low $Re_m$ assumption) is solved for simple and complex geometries with imposed magnetic fields. MHD flow control dynamics were validated in line with literature results and complex double cone flows with shock wave boundary layer interaction and real gas chemistry were effectively captured as compared with available experimental data.

The model employs a highly efficient implementation whereby plasma19 EoS leverages pre-computed state data, and geometry is modelled via an embedded boundary Ghost Fluid Method, this facilitates an underlying mesh consisting of hierarchical AMR within the AMReX framework which offers a very high degree of parallelism and scalability. On equivalent meshes, the model run time is close (within 24%) to the efficiency of the simple ideal gas model often employed in previous studies for its ease of computation. Unlike equivalent ideal gas models, this model is able to directly compute electron number density and electrical conductivity, which are important for the prediction of plasma properties and MHD effects.

Simulations were produced of the experimental test conditions producing a non-simple shock structure around a double-cone geometry under electrodynamic influence. Numerical results were produced in line with experiments for shock structure and increase in stand-off distance, therefore improving upon previous numerical predictions which could not resolve an MHD effect for the experimental value of magnetic field intensity.

There are many other MHD applications of interest under this regime, with high relevance to emerging flight control and reusable space technologies.

**Acknowledgements.** I (H.A. Muir) would like to acknowledge the General Sir John Monash Foundation and the Laboratory for Scientific computing, by whom the work has been funded. I would also like to acknowledge and thank Leoni Pugh for working with us to develop Fig. 1 of this paper.

## References

1. Bityurin, V.A., Bocharov, A.N.: MHD flow control in hypersonic flight. In: AIAA/CIRA 13th International Space Planes and Hypersonics Systems and Technology. Institute for High Temperatures of Russian Academy of Sciences, Moscow, Russia (2005)
2. Edwards, T.A.: Fluid/chemistry modeling for hypersonic flight analysis. Comput. Math. Appl. **24**(5–6), 25–36 (1992)
3. Chalot, F., Hughes, T.J.: A consistent equilibrium chemistry algorithm for hypersonic flows. Comput. Methods Appl. Mech. Eng. **112**(1–4), 25–40 (1994)
4. Sawada, K., Dendou, E.: Validation of hypersonic chemical equilibrium flow calculations using ballistic-range data. Shock Waves **11**(1), 43–51 (2001)

5. Lani, A., Molnar, J., Abeele, D.V., Rini, P., Magin, T., érard Degrez, G.: Numerical study of elemental demixing in atmospheric entry flow regimes near local thermodynamic equilibrium. In: European Conference on Computational Fluid Dynamics, Von Karman Institute for Fluid Dynamics (VKI), Aeronautics and Aerospace Department (2006)
6. Fujino, T., Ishikawa, M.: Numerical simulation of control of plasma flow with magnetic field for thermal protection in earth reentry flight. IEEE Trans. Plasma Sci. **34**(2) (2006)
7. Anderson, J.D.: Hypersonic and High Temperature Gas Dynamics. McGraw-Hill, New York (1989)
8. Savino, R., Paterna, D., De Stefano Fumo, M., D'Elia, M.: Plasma-radiofrequency interactions around atmospheric re-entry vehicles: modelling and arc-jet simulation. Open Aerosp. Eng. J. **3**, 76–85 (2010)
9. Bisek, N.J.: Numerical study of plasma-assisted aerodynamic control for hypersonic vehicles, Ph.D. thesis, Department of Aerospace Engineering, The University of Michigan (2010)
10. D'Angola, A., Colonna, G., Gorse, C., Capitelli, M.: Thermodynamic and transport properties in equilibrium air plasmas in a wide pressure and temperature range. Eur. Phys. J. D **46**, 129–150 (2008)
11. D'Angola, A., Colonna, G., Gorse, C., Capitelli, M.: Thermodynamic properties of high temperature air in local thermodynamic equilibrium: II accurate analytical expression for electron molar fractions. Eur. Phys. J. D **65**, 453–457 (2011)
12. Träuble, F., Millmore, S., Nikiforakis, N.: An improved equation of state for air plasma simulations. Phys. Fluids **33**(3), 036112 (2021)
13. Goedbloed, J.P., Poedts, S.: Principles of Magnetohydrodynamics: With Applications to Laboratory and Astrophysical Plasmas. Cambridge University Press, Cambridge (2004)
14. Dias, F., Xisto, C.: Numerical computations of MHD flow on hypersonic and reentry vehicles. In: Proceedings of the ASME 2018 IMECE (2018)
15. Fujino, T., Matsumoto, Y., Kasahara, J., Ishikawa, M.: Numerical studies of magnetohydrodynamic flow control considering real wall electrical conductivity. J. Spacecraft Rockets **44**(3), 625–632 (2007)
16. Otsu, H., Konigorski, D., Abe, T.: Influence of hall effect on electrodynamic heat shield system for reentry vehicles. AIAA J. **48** (10)
17. Matsuda, A., Otsu, H., Kawamura, M., Konigorski, D., Takizawa, Y., Abe, T.: Model surface conductivity effect for the electromagnetic heat shield in re-entry flight. Phys. Fluids 20 (2008)
18. Poggie, J., Gaitonde, D.V.: Magnetic control of flow past a blunt body: numerical validation and exploration. Phys. Fluids 1**14**, 127103 (2008)
19. Khan, O.U., Hoffmann, K.A., Dietiker, J.: Computational aspects of high-speed flows with applied magnetic field. IEEE Trans. Magn. **42**(3), 389–397 (2006)
20. Yoshino, T., Fujino, T., Ishikawa, M.: Possibility of thermal protection in earth re-entry flight by MHD flow control with air-core circular magnet. Trans. Electr. Electron. Eng. (4), 510–517 (2009)
21. Colonna, G.: Improvements of hierarchical algorithm for equilibrium calculation. Comput. Phys. Commun. **177**, 493–499 (2007)
22. Asinovsky, E., Kirillin, A., Pakhomov, E., Shabashov, V.: Experimental investigation of transport properties of low-temperature plasma by means of electric arc. Proc. IEEE **59**(4), 592–601 (1971)
23. Schreiber, P., Hunter, A., Benedetto, K.: Electrical conductivity and total emission coefficient of air plasma. AIAA J. **11**(6), 815–821 (1973)

24. Yos, J.: Transport properties of nitrogen, hydrogen, oxygen, and air. AVCO/RAD-TM **63**(7) (1963)
25. Bush, W.B.: Magnetohydrodynamic-hypersonic flow past a blunt body. J. Aerosp. Sci. **25**(11), 685–690 (1958)
26. Villa, A., Malgesini, R., Barbieri, L.: A multiscale technique for the validation of a numerical code for predicting the pressure field induced by a high-power spark. J. Phys. D Appl. Phys. **44** (165201)
27. Almgren, A., Bell, J. (primary developers): AMReX - a software framework for massively parallel, block-structured adaptive mesh refinement (AMR) applications, opensource (2020). https://amrex-codes.github.io/amrex/
28. Bennett, W.P., Michael, L., Nikiforakis, N.: Cartesian cut-cell and GFM approaches to free-surface and moving boundary interaction. In: 54th AIAA Aerospace Sciences Meeting 0602 (2016)
29. Sambasivan, S.K., UdayKumar, H.S.: Ghost fluid method for strong shock interactions part 2: immersed solid boundaries. AIAA **47**(12), 2923–293 (2009)
30. Tramel, R., Nichols, R., Buning, P.: Addition of improved shock-capturing schemes to overflow 2.1, p. 3988 (2009)
31. Damevin, H.-M., Hoffmann, K.A.: Numerical simulations of magnetic flow control in hypersonic chemically reacting flows. J. Thermophys. Heat Transf. **16**(4), 498–507 (2002)
32. Fujino, T., Matsumoto, Y., Kasahara, J., Ishikawa, M.: Numerical analysis of reentry trajectory coupled with magnetohydrodynamics flow control. J. Spacecraft Rockets **45**(5), 911–920 (2008)
33. Holden, M., Wadhams, T., Boyd, I., Wang, W.: CFD validation for hyperconic flight: hypersonic double-cone flow simulations. In: 40TH AIAA Aerospace Sciences Meeting and Exhibit, Reno, NV, pp. 14–17 (2002)
34. Hao, J., Wang, J., Lee, C.: Numerical simulation of high-enthalpy double-cone flows. AIAA J. **55**(7), 2471–2475 (2017)
35. Hao, J., Wen, C.-Y.: Numerical investigation of oxygen thermochemical nonequilibrium on high-enthalpy double-cone flows. Int. J. Heat Mass Transf. **127**, 892–902 (2018)
36. Zuo, F.-Y., Hu, S.-L.: Thermochemical non-equilibrium effects on aerothermodynamic prediction of laminar double-cone flow. Acta Astronautica (2021)
37. Holloway, M.E., Hanquist, K.M., Boyd, I.D.: Assessment of thermochemistry modeling for hypersonic flow over a double cone. J. Thermophys. Heat Transf. **34**(3), 538–547 (2020)
38. Nagata, Y., Yamada, K., Abe, T.: Numerical investigation of the electrodynamic flow control around the double-cone configuration. In: 49th AIAA Aerospace Sciences Meeting including the New Horizons Forum and Aerospace Exposition (2011)
39. Moss, J.N., Bird, G.A.: Direct simulation Monte Carlo simulations of hypersonic flows with shock interactions. AIAA J. **43**(12), 2565–2573 (2005)
40. Wasai, K., Makino, H., Nagata, Y., Hiraoka, K., Yamada, K., Abe, T.: Electrodynamic control of shock interactions in a 25°/55° double cone model in hypersonic flow. In: 48th AIAA Aerospace Sciences Meeting Including the New Horizons Forum and Aerospace Exposition (2010)
41. Nagata, Y., Yamada, K., Abe, T.: Hypersonic double-cone flow with applied magnetic field. J. Spacecraft Rockets **50**(5), 981–991 (2013)